Cassini Observes the Active South Pole of Enceladus

C. C. Porco, *et al.*

Science **311**, 1393 (2006);
DOI: 10.1126/science.1123013

Science (print ISSN 0036-8075; online ISSN 1095-9203) is published weekly, except the last week in December, by the American Association for the Advancement of Science, 1200 New York Avenue NW, Washington, DC 20005.

RESEARCH ARTICLE

Cassini Observes the Active South Pole of Enceladus

C. C. Porco,[1*] P. Helfenstein,[2] P. C. Thomas,[2] A. P. Ingersoll,[3] J. Wisdom,[4] R. West,[5] G. Neukum,[6] T. Denk,[6] R. Wagner,[7] T. Roatsch,[7] S. Kieffer,[8] E. Turtle,[9] A. McEwen,[9] T. V. Johnson,[5] J. Rathbun,[10] J. Veverka,[2] D. Wilson,[1] J. Perry,[9] J. Spitale,[1] A. Brahic,[11] J. A. Burns,[2] A. D. DelGenio,[12] L. Dones,[13] C. D. Murray,[14] S. Squyres[2]

Cassini has identified a geologically active province at the south pole of Saturn's moon Enceladus. In images acquired by the Imaging Science Subsystem (ISS), this region is circumscribed by a chain of folded ridges and troughs at ~55°S latitude. The terrain southward of this boundary is distinguished by its albedo and color contrasts, elevated temperatures, extreme geologic youth, and narrow tectonic rifts that exhibit coarse-grained ice and coincide with the hottest temperatures measured in the region. Jets of fine icy particles that supply Saturn's E ring emanate from this province, carried aloft by water vapor probably venting from subsurface reservoirs of liquid water. The shape of Enceladus suggests a possible intense heating epoch in the past by capture into a 1:4 secondary spin/orbit resonance.

Within 6 months of entering Saturn orbit on 1 July 2004 UTC, the Cassini spacecraft began a year of intense examination of the major icy satellites of Saturn. Between 15 December 2004 and 24 December 2005, Cassini executed 21 satellite flybys, including 7 flybys with closest approaches within 1500 km. Of all of these, the most eagerly anticipated were those of Enceladus.

At 504 km in diameter, Enceladus orbits between Mimas and Tethys. A mean motion resonance with Dione excites its orbital eccentricity of 0.0047. It has long been known to have peculiar surface properties, and its visual geometric albedo of 1.4 (*1*) makes it one of the brightest satellites in the solar system, with a reflectance spectrum dominated by pure water ice (*2*). Enceladus' association with the E ring, and the very narrow size distribution of particles constituting the E ring, suggested possible present-day venting or geyser-like activity (*3*) and subsequent coating of the moon by E-ring particles. Voyager images also provided high-resolution (~1 km/pixel) coverage, primarily of the northern hemisphere of Enceladus, with some lower resolution observations extending downward to mid-southern latitudes, showing that its surface is divided into morphologically diverse geological provinces that document a long and complex history (*4*–*6*). Bowl-shaped craters dot the heavily cratered, oldest terrains; craters elsewhere showed evidence for viscous relaxation. Other regions displayed narrow linear ridges with kilometer-scale relief, as well as fractures overprinting other fractures. The youngest visible regions appeared smooth. Voyager coverage near the south polar region was sparse and poorly resolved.

Pre-Cassini studies of Enceladus' thermal history and interior structure focused on explaining the viscous relaxation and extensive resurfacing suggested by Voyager images (*4*). The goal of previous models was to investigate ways of producing, at some recent epoch, global interior temperatures at or close to the water ice melting point, allowing possible cryovolcanism, subsolidus convection, and near-surface viscous relaxation of impact structures. Post-Voyager thermal history studies concluded that it was impossible to reach the melting point of pure ice under the current physical conditions (*5*). However, the presence of ammonia, which can exist with water as a eutectic melt at absolute temperatures $T \sim 175$ K, was suggested as a means to lower the temperature (*7*) and melt the interior (*5*). Cryovolcanic activity driven by water-ammonia became a plausible resurfacing mechanism. Models invoking Enceladus' orbital evolution and the possibility of intense tidal heating in the past have also been examined [e.g., (*8*)]. On the basis of Voyager-era estimates of the shape of Enceladus, a 1:3 spin/orbit resonance was postulated as being capable of producing sufficient present-day heat to melt the interior (*9*), although it required that Enceladus be undergoing a forced libration of several degrees amplitude.

Cassini flybys. Because of its uniqueness among saturnian moons, three very close Cassini encounters of Enceladus were executed in 2005 to gather information on its physical characteristics, magnetic and plasma environment, and geologic activity (if any). The first encounter on 17 February 2005 saw approach on the trailing hemisphere and brought the spacecraft within 1259 km over the Saturn-facing equatorial region of the moon during closest approach. This flyby resulted in the first detection, by the Cassini Magnetometer, of a tenuous atmosphere around Enceladus distorting Saturn's magnetic field lines (*10*), and confirmed [by the Visual and Infrared Mapping Spectrometer (VIMS)] a surface dominated by water, with simple organics and CO_2 coincident with prominent fractures seen in the south polar region (*11*). Surface NH_3 was not detected. Imaging Science Subsystem (ISS) images acquired during this flyby in both clear and spectral filters (*12*) revealed the "smooth" plains seen by Voyager to be finely fractured.

The second closest approach took place on 9 March 2005, at a distance of 497 km above the anti-Saturn equatorial region. The magnetic signature during this flyby confirmed a southerly atmospheric source of water-ion mass loading of the plasma around Enceladus.

The third flyby of Enceladus on 14 July 2005 was lowered to a close-approach distance of 168 km (well within Enceladus' Hill radius of ~950 km) to allow high-resolution investigation with both remote sensing and in situ instruments of the southern polar environment. Very high resolution images of the south polar terrains, as well as some extremely high resolution images acquired during this event (with image scales as fine as 4 m/pixel), revealed a landscape near the south pole littered with house-sized ice boulders, carved by tectonic features unique to Enceladus, and almost entirely free of impact craters. Several prominent, ~130-km-long fractures dubbed "tiger stripes" were seen straddling the south pole; the region south of ~55°S latitude was circumscribed by an unusual continuous chain of sinuous fractures and ridges. The Cassini Composite Infrared Spectrometer (CIRS) found the south polar region to be anomalously warm (*13*); comparison of the thermal and imaging results revealed the highest graybody temperatures observed on Enceladus, between 114 and 157 K, to be coincident with the prominent tiger stripe fractures crossing the south pole (*14*).

The July encounter produced unequivocal evidence of a plume of water vapor and small icy particles emanating from the south polar region of Enceladus (*15*–*18*) (Fig. 1). Surprisingly, the Ion and Neutral Mass Spectrometer (INMS)

[1]Cassini Imaging Central Laboratory for Operations, Space Science Institute, 4750 Walnut Street, Suite 205, Boulder, CO 80301, USA. [2]Department of Astronomy, Cornell University, Ithaca, NY 14853, USA. [3]Division of Geological and Planetary Sciences, California Institute of Technology, 150-21, Pasadena, CA 91125, USA. [4]Department of Earth, Atmospheric, and Planetary Sciences, Massachusetts Institute of Technology, Cambridge, MA 02139, USA. [5]Jet Propulsion Laboratory, California Institute of Technology, Pasadena, CA 91109, USA. [6]Institut für Geologische Wissenschaften, Freie Universität, 12249 Berlin, Germany. [7]Institute of Planetary Research, German Aerospace Center, Rutherfordstrasse 2, 12489 Berlin, Germany. [8]Department of Geology, University of Illinois, Urbana, IL 61801, USA. [9]Department of Planetary Sciences, University of Arizona, Tucson, AZ 85721, USA. [10]Department of Physics, University of Redlands, 1200 East Colton Avenue, Redlands, CA 92373, USA. [11]Centre d'Etudes de Saclay, Université Paris 7, L'Orme des Merisiers, 91191 Gif-sur-Yvette Cedex, France. [12]Goddard Institute for Space Studies, NASA, 2880 Broadway, New York, NY 10025, USA. [13]Department of Space Studies, Southwest Research Institute, 1050 Walnut Street, Suite 400, Boulder, CO 80302, USA. [14]Astronomy Unit, Queen Mary, University of London, London E1 4NS, UK.

*To whom correspondence should be addressed. E-mail: carolyn@ciclops.org

detected no gaseous NH_3 (*16*). On the basis of these findings, very high phase angle, high-resolution ISS imaging sequences were executed on 27 November 2005 specifically to examine the plume over the south pole.

We discuss here the results of analyses of ISS images of the south polar environment of Enceladus. Images taken as early as 16 January 2005, images acquired during the February and July 2005 flybys, and those taken in late November 2005 have yielded striking visual evidence of many narrow jets of fine icy particles emanating from the south polar terrain (SPT) feeding a large plume over the south pole. They have also yielded indications of extreme geologic youth in the SPT, morphological evidence of a change over time in surface stresses in the southern hemisphere, and possible evidence of an epoch of intense heating in the past. Moreover, recent Cassini imaging and spacecraft tracking data, as well as up-to-date dynamical modeling of the entire Saturnian satellite system, have substantially improved the accuracy of the Enceladus mass density, and therefore radiogenic heating estimates, since the Voyager flybys. Enceladus' interior is clearly warmer and more dissipative than most previous interior models have predicted. All these new results have motivated a re-evaluation of the past and present state of the moon's interior, with the seemingly unavoidable conclusion that the standard, spherically symmetric thermal models of Enceladus' interior do not apply.

South polar terrain. The SPT of Enceladus is distinguished by its tectonic patterns, youthful geology, and unusual albedo and color patterns. The region is disrupted by complex fracture patterns and separated from the rest of Enceladus by a continuous sinuous chain of scarps, parallel ridges, and troughs at ~55°S latitude and covers an area of about 70,000 km^2 (about 9% of Enceladus' surface; Fig. 2). This boundary is interrupted in several places by "Y-shaped" discontinuities (Fig. 2, A, B, and D) that taper northward. These features transition toward the equator to subparallel networks of north-south–trending rifts and cracks that are the youngest features on these terrains (Fig. 2, A and D). The south-facing openings of the Y-shaped discontinuities confine parallel chains of convex-northward curved ridges and troughs (Fig. 2, A, B, and D). ISS stereo images and oblique views of the confined fold belts show that they are hundreds of meters higher than surrounding terrain. These curved forms can best be interpreted as fold belts resulting from horizontal compression.

The interior of the SPT is characterized by a complex network of cross-cutting fractures. Most conspicuous is a family of roughly parallel lineaments that we informally term "tiger stripes" (Fig. 3A). ISS images show that the tiger stripes are linear depressions, typically about 500 m deep, 2 km wide, and 130 km in length, flanked on both sides by prominent 100-m-high ridges (Fig. 2C; Fig. 3, B and C). Darker material extends a few kilometers to either side. They are spaced ~35 km apart and have similar shapes and orientations, with strike directions ~45° offset from the Saturn direction (longitude 0°; Fig. 2A). In the anti-Saturn hemisphere (longitude 180°), tiger stripes often terminate in prominent hook-shaped bends, but in the sub-Saturn hemisphere, they progressively bifurcate into crudely dendritic patterns (Fig. 3C).

The spectrophotometry of the SPT is unusual on Enceladus. At low phase, the bright plains in between the tiger stripes are ~10% brighter than the average reflectivity of Enceladus (Fig. 3A); the contrast between these units and the tiger stripes is ~20% and the greatest seen on Enceladus. These distinct properties may be directly related to the geologic activity, present-day venting, and particle fallout ongoing in this region (see below). ISS broadband spectra of all SPT materials (fig. S1A) are consistent with a composition of pure water ice. However, although the very bright interstripe plains show almost flat spectra, indicative of grain sizes on the order of tens of micrometers (*19*) (fig. S1B), the tiger stripes' spectra show stronger absorptions consistent with larger grain sizes of ~100 μm. ISS multispectral measurements alone do not indicate whether the coarse-grained ice consists of a surface deposit of ~100-μm particles, boulders composed of coarse-grained ice crystals, relatively bare outcrops of solid ice, or some other morphology. Elsewhere on Enceladus we find coarse-grained icy material, also in association with pristine fractures, in rather limited areas on fracture walls. This too may be exposed solid ice. Narrow deposits of spectrally distinct icy material that often thread along the valley floors (Fig. 3B) may indicate icy blocks that have broken loose from fracture walls. The

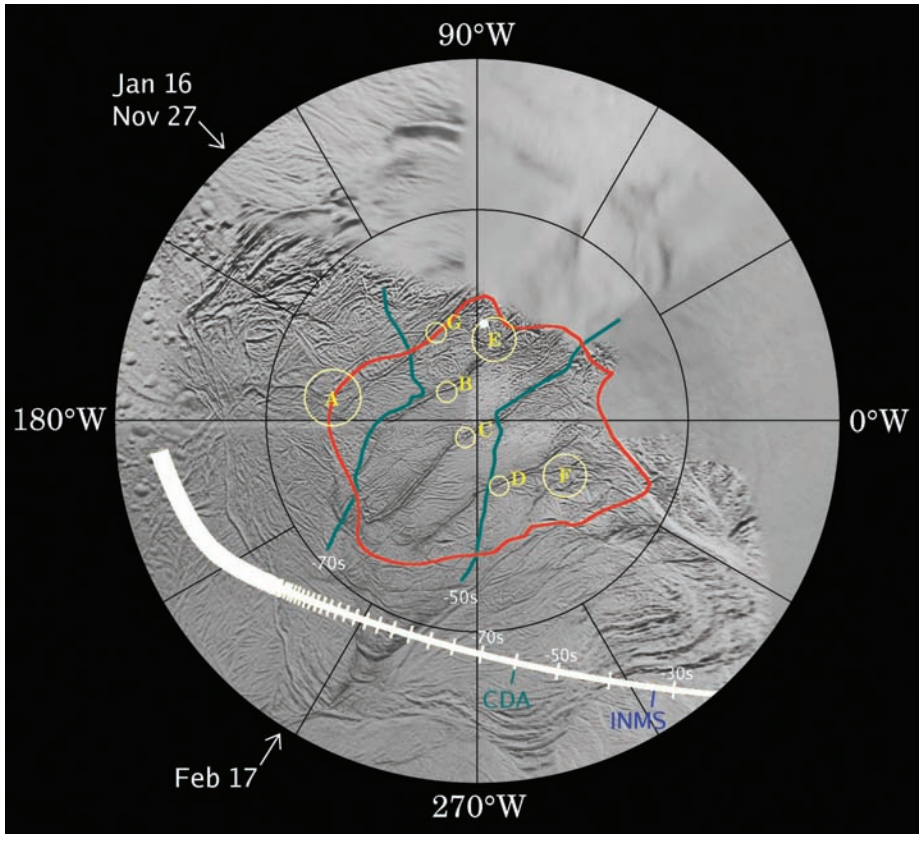

Fig. 1. Observations and model results from a suite of Cassini instruments projected onto a polar stereographic base map of the 30° to 90°S latitude portion of the southern hemisphere of Enceladus. The flight path of Cassini, marked by seconds from closest approach, during the 11 July 2005 flyby is indicated, along with the locations of the position of the spacecraft when the CDA particle (*15*) and INMS vapor (*16*) counts peaked. The spacecraft altitude at these positions was ~400 km and ~250 km, respectively. The contours enclosing the source regions of particles arriving at Cassini from within the SPT at –50 s and –70 s from closest approach, as modeled by the CDA experiment, are drawn in green. The single white dot is the intersection with the limb of the path of γ-Orionis seen from the UVIS experiment (*17*). The contour enclosing brightness temperatures hotter than 77 K as measured by CIRS is shown in orange; the seven hottest measured locales, A through G, are shown in yellow (*13*). The "look" directions for the ISS plume observations on 16 January, 17 February, and 27 November are indicated by arrows.

tiger stripes have sharp relief and cross-cut all other fractures in their path. This, together with their color and coarse grain size, is evidence of geologic youth.

Most of Enceladus' bright surface (Fig. 3A) is likely derived from a covering of fine-grained regolith that has accumulated over time as a result of impact comminution, especially by high-velocity E-ring particles and perhaps sputtering redistribution. The absence of such a covering on the tiger stripes is consistent with the interpretation that the tiger stripe material was either emplaced too recently to have accumulated such a regolith or has undergone thermal processing (such as thermal metamorphosis of ice grains) or both. The high temperatures of the tiger stripes (*13*) strongly suggest that warm conditions and active venting may be responsible for their crystallinity and other spectrophotometric attributes.

The highest resolution images of the SPT, with nominal image scales of 38 and 3.8 m/pixel (Fig. 3, D and E), show a hummocky or block-covered surface between trough-like expressions of crossing fractures. The color within this region is a patchy mixture of bluish tiger stripe material and whiter ice, and may be a transitional unit. Most blocks in this unit are between 20 and 50 m across; a few are as large as 100 m. The high fraction of the surface covered by the blocks, and the lack of any craters within tens of kilometers, suggests a formation mechanism other than crater ejecta, such as tectonic or seismic disruption of a highly fractured surface layer. Erosional mechanisms, such as sublimation and particle bombardment, may have further modified them.

The SPT that surrounds and predates the tiger stripes is morphologically and stratigraphically complex. Local patterns of fractures vary from straight orthogonal sets, some showing

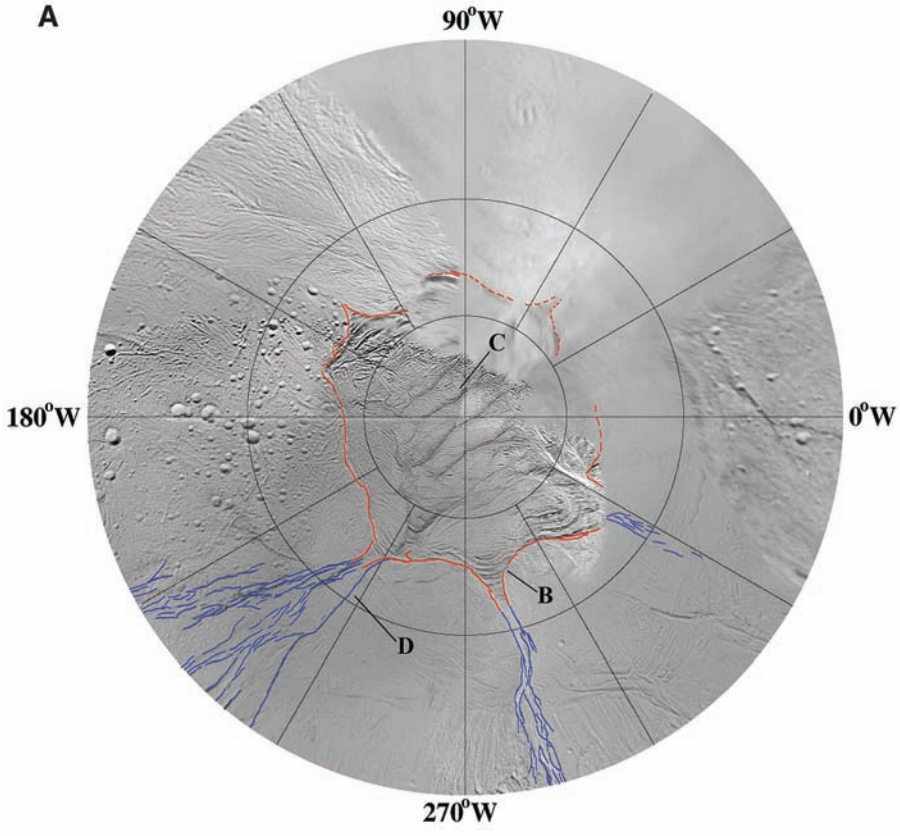

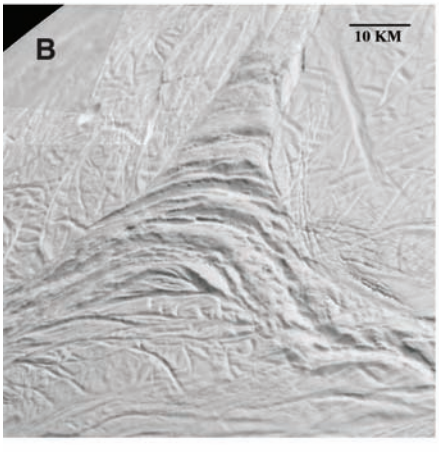

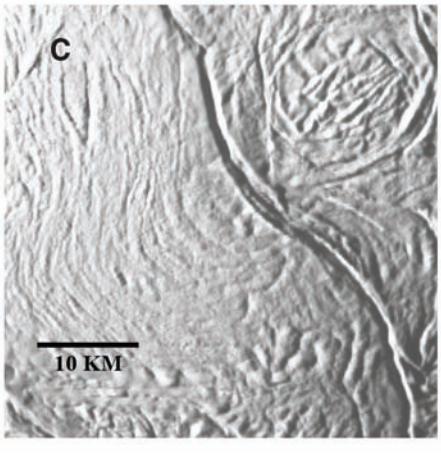

Fig. 2. (**A**) Polar stereographic basemap of the SPT covering latitudes from 0° to 90°S. The basemap also shows details obtained from the best ISS coverage of Enceladus' SPT to date. The circumpolar tectonic margin that encloses the SPT is marked as solid red lines where it is well resolved in high-resolution ISS images and as dashed red lines where it is interpreted from low-resolution coverage. Blue lines identify prominent, young tension fractures that extend from the Y-shaped discontinuities north to the equator. (**B**) Morphological details of a Y-shaped discontinuity along the SPT margin near 44°S, 279°W. North is up and the image scale is 70 m/pixel. (**C**) Example of grooved bands in bright plains adjacent to a tiger stripe at 86°S, 102°W. Note how the bands curve to define a quasi-circular feature. (**D**) Transition of Y-shaped discontinuity at the polar terrain boundary near 30°S, 229°W to north-south–trending fractures extending to the equator (blue lines in Fig. 3A).

apparent lateral shear offsets, to highly reticulated patterns of grooves and ridges. Grooved bands (Fig. 2C) with tens to 100 m of relief often curve parallel to bends in adjacent tiger stripes. However, in some locations, they deflect and arc to form quasi-circular patterns that may represent relaxed and degraded impact craters. Alternatively, these quasi-circular patterns may be surface expressions of subsurface diapirs.

Cratering statistics. Crater counts on Enceladus were obtained from images acquired during the February, March, and July 2005 flybys. Of all saturnian satellites investigated so far [e.g., (*20*–*22*)], Enceladus has the largest range in crater number density, implying a record of long-lasting, possibly still ongoing, geologic activity (Fig. 4). Heavily and moderately cratered regions are found outside the SPT, in places dissected by isolated or densely spaced sets of fractures and troughs, or ridges and grooved bands (Table 1). The lowest crater densities on Enceladus were measured in the SPT near the tiger stripes. Here, only a small number of craters occur, none larger than 1 km.

The cratering frequencies are roughly consistent with impacts of bodies in moderately eccentric planetocentric orbits (*23*–*25*). Scaling the impactor fluxes from Iapetus to Enceladus under two different flux scenarios (Table 1), and accounting for the derived age of the Iapetus surface (*21*), the derived absolute ages for terrains on Enceladus from crater counts strongly indicate geologic activity over a time span of more than 4 billion years up to the present. Ages within the SPT are possibly as young as 500,000 years or younger. The discrete ages of different terrains suggests that rather than being continuously active through geologic time, Enceladus experienced localized episodes of activity perhaps separated by much longer time periods of inactivity.

Shape and density. The shape of Enceladus has been determined from limb profiles in 23 narrow-angle images. The satellite is well represented by an ellipsoid with semi-axes 256.6 ± 0.5, 251.4 ± 0.2, and 248.3 ± 0.2 km. Knowledge of the mass of Enceladus has been improved over Voyager-era estimates by the use of astrometric measurements taken from Cassini as well as historical Earth-based, Hubble Space Telescope, and Voyager images, together with dynamical modeling of the bodies in the Saturn system and spacecraft tracking data from the Pioneer, Voyager, and Cassini missions (*26*). Adopting the most recent value derived from these methods [$GM = 7.2085 \pm 0.0068$ km^3 s^{-2} (*27*), where GM is Newton's gravitational constant times the mass of Enceladus], and using the effective radius of 252.1 ± 0.2 km derived from ISS images, we compute a mean density for Enceladus of 1608.3 ± 4.5 kg m^{-3}. Enceladus shows a total range of departures from the mean ellipsoid of ~2 km. Longitudinally averaged limb heights rise from 400 m below the reference ellipsoid at the south pole to 400 m above it at 50°S latitude. If Enceladus is homogeneous throughout, then its shape is close to that of an equilibrium ellipsoid (i.e., one with a hydrostatic shape controlled by gravity and spin). An object hydrostatically relaxed in synchronous spin at Enceladus' orbit would have a difference of long and short axes of 8.05 km (*28*), within our uncertainty of 0.6 km of the measured 8.3 km.

The intermediate (b) axis is too large for an exact equilibrium shape, and if homogeneous, Enceladus currently supports between 250 and 500 m of topography relative to an equipotential surface. We conclude that Enceladus' shape is consistent with relaxation of a homogeneous object of density 1608 kg m^{-3} at its current or-

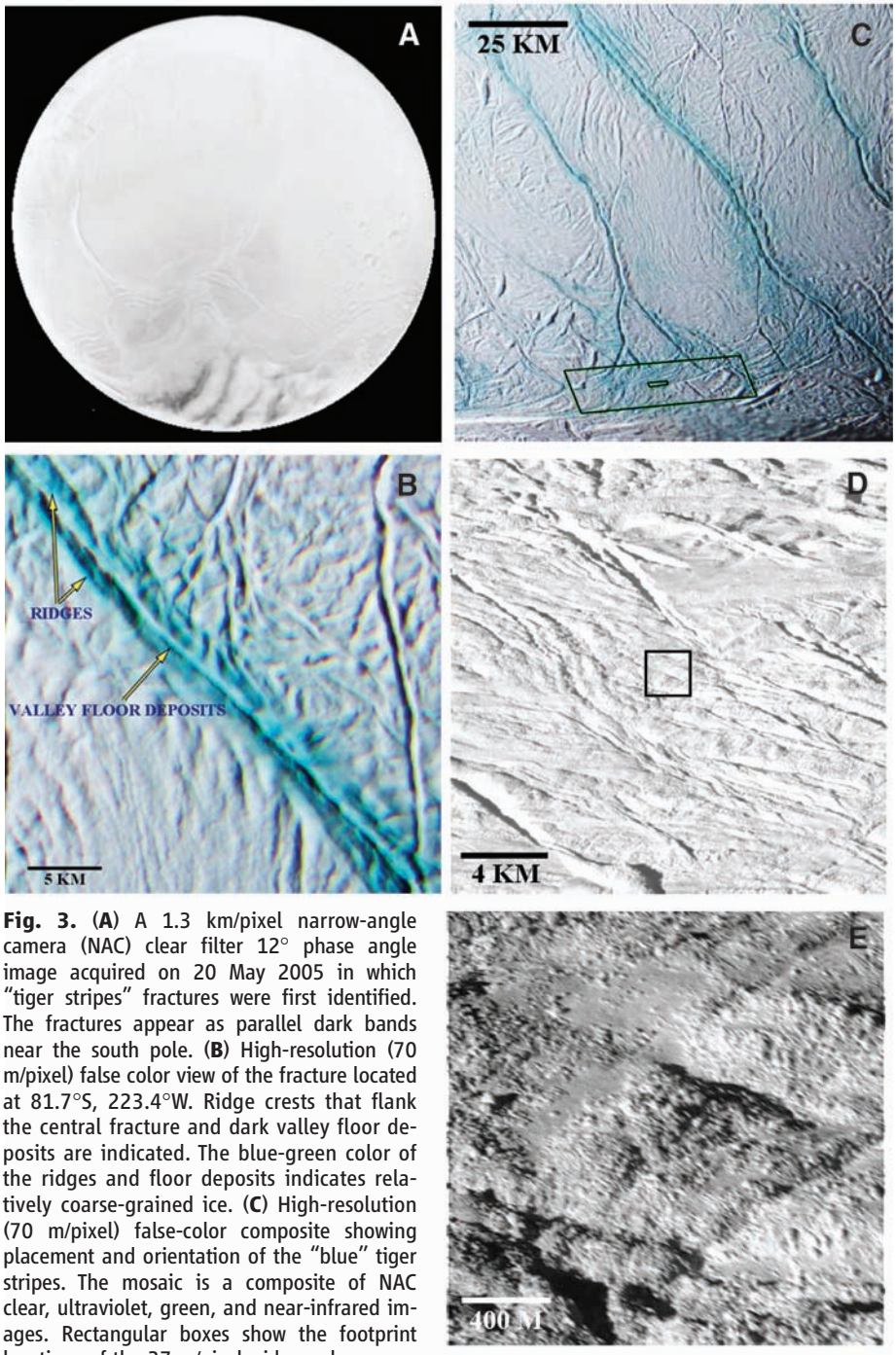

Fig. 3. (**A**) A 1.3 km/pixel narrow-angle camera (NAC) clear filter 12° phase angle image acquired on 20 May 2005 in which "tiger stripes" fractures were first identified. The fractures appear as parallel dark bands near the south pole. (**B**) High-resolution (70 m/pixel) false color view of the fracture located at 81.7°S, 223.4°W. Ridge crests that flank the central fracture and dark valley floor deposits are indicated. The blue-green color of the ridges and floor deposits indicates relatively coarse-grained ice. (**C**) High-resolution (70 m/pixel) false-color composite showing placement and orientation of the "blue" tiger stripes. The mosaic is a composite of NAC clear, ultraviolet, green, and near-infrared images. Rectangular boxes show the footprint locations of the 37 m/pixel wide-angle camera (WAC) (larger box) and 4 m/pixel NAC (smaller box) images shown in (D) and (E), respectively. (**D**) WAC 37 m/pixel image obtained at the distal edge of a tiger stripe [see (C)]. Central square shows location of co-aligned NAC 4 m/pixel image shown in (E). (**E**) Highest spatial scale (4 m/pixel) image ever obtained of Enceladus' surface. Image exhibits several pixels of smear from left to right because of spacecraft motion.

bital distance. Models with thin ice crusts are also indistinguishable from hydrostatic shapes. A core of density 1700 kg m^{-3} requires an ice crust of thickness ~10 km; a core density of 1800 kg m^{-3} requires a crust of ~20 km. Within the uncertainties, both also support topography under 500 m and can be regarded as consistent with relaxation under current conditions (Table 2).

However, a fully differentiated Enceladus with a water-ice mantle and a core of density 2700 kg m^{-3} would exhibit a departure from a fully relaxed, hydrostatic shape of more than a kilometer. A differentiated body with such relief must have relaxed at a higher rotation rate than at present. If orbitally evolved, this would place its relaxation between 0.87 and 0.95 of Enceladus' current orbital distance. Denser, smaller cores would require shape equilibration even closer to Saturn. However, standard orbit evolution models indicate that the orbit of Enceladus could not have changed more than 5%, which suggests that it mostly likely formed within 95% of its current location (*29*). Moreover, orbital evolution outward would push the shape of a warm body toward a less oblate, more hydrostatic form, inconsistent with the tectonic patterns seen on the surface (which suggest progression, at least in the southern hemisphere, to a more oblate shape; see below). Hence, whether homogeneous or not, Enceladus probably did not undergo substantial orbital evolution.

The shape of the moon is also important for ascertaining its rotation state. Table 2 gives the moments of inertia for all four interior models mentioned above. In all four cases, the moments yield a ratio of libration frequency to spin frequency $\varepsilon = [3(B - A)/C]^{1/2} \sim 0.25$; this value raises the question of whether Enceladus is currently in a forced 1:4 secondary spin-orbit libration, or has been in the past (*9*). To search for present-day libration, we have obtained 1375 measurements of 190 control points in 129 images that span more than half of Enceladus' orbit with respect to periapse and have fitted these with a model describing the 1:4 spin/orbit libration. No libration was detected. The uncertainties in the solution yield a libration amplitude upper limit of 1.5°. Limb-fitting results require the long axis to point within 5° of Saturn.

Particle plumes. Plumes emanating from the south polar region of Enceladus have been detected in ISS high phase angle images. One relatively large, near-surface plume was seen in images taken on 16 January 2005 at a phase angle of 148° (Fig. 5A). Near-surface plumes were again detected on 17 February 2005 at a phase angle of 153.3°; a fainter, much more extended component is also visible at this phase angle (Fig. 5B, right). Finally, very high phase angle (161.4°) images were taken on 27 November 2005 (Fig. 6) and reveal many distinct near-surface jets, emanating from the surface in a variety of directions and supplying a much bigger, fainter plume towering over the south polar region by at least 435 km. The fact that these structures were seen at high rather than low phase angles indicates that they consist of fine, forward-scattering particles. The source regions of these jets inferred from triangulation appear to be consistent with the tiger stripes.

Absolute brightness measurements, and hence particle column densities (*30*), were obtained in the photometrically calibrated versions of the high-resolution November images over a range of heights and azimuths above the moon's south polar limb to determine the profile of particle number density with altitude, as well as the particle escape rate integrated over the extended plume. In all three image sequences—January, February, and November—the scale heights within ~50 km of the surface are ~30 km; the fall-off becomes more gradual above that point. In the November images, the brightness profile up to one Enceladus radius above the surface fits a model in which the vertical velocity v has a Gaussian distribution [i.e., proportional to $\exp(-v^2/v_0^2)$]; the other velocity components are zero. The particles move vertically, perpendicular to the orbit plane, in the gravitational field of Enceladus; the tidal field of Saturn does not affect motions in this direction. The best fit gives a mean vertical velocity $v_0/\pi^{1/2} = 60$ m s^{-1}. This is much less than the

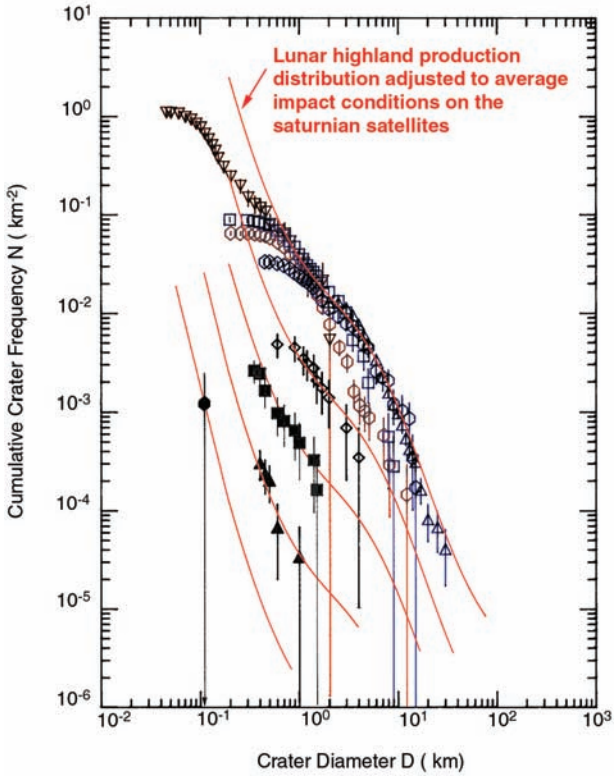

Fig. 4. Cumulative crater size-frequency distributions of geologic units measured on Enceladus. The five sets of distributions correspond to the units listed in Table 1. Curve shown is the lunar highland distribution. The shape of the lunar curve is compatible with the measurements if crater diameters are shifted by about a factor of 5 to smaller values with respect to lunar conditions. Uppermost (oldest) distributions are from heavily cratered plains. Black (open) diamonds correspond to striated and folded plains within Sarandib Planitia. Black solid dots represent distributions measured in the SPT. The single dot is the estimation of a maximum crater age for the single 37 m/pixel WAC frame.

Table 1. Location of crater counting areas (geologic units) and crater frequency ratios (*N*-ratios, where *N* is cumulative crater frequency) of counts with respect to a hypothetical surface of age 4.4 × 10^9 years on Enceladus. Geologic units were identified and mapped at regional scales of ~100 m/pixel; a single WAC frame (37 m/pixel; Fig. 3D) obtained during the July flyby was also measured. In areas II and III, no craters larger than ~5 km were found. The ages are derived for two scenarios: a lunar-like impact chronology with steep initial decay (*23*, *25*, *43*) and a constant-flux model of cometary impacts (*44*).

Geologic unit and location	*N*-ratio	Age (10^6 years) (lunar-like)	Age (10^6 years) (constant flux)
I. Heavily cratered plains (15° to 45°N, 340° to 360°W; 20°N to 30°S, 160° to 210°W)	1/4.7	4200	1700
II. Striated and folded plains in Sarandib Planitia (15°N to 5°S, 305° to 320°W)	1/70	3750	170
III. Ridged and grooved plains in Samarkand Sulcus (55° to 65°S, 170° to 240°W)	1/1170	980	10
IV. South Polar Terrain (>55°S, 160° to 320°W)	1/10,770	100	1
V. Single WAC frame within SPT 37 m/pixel (350°W, 75°S)	<1/311,000	<4	<0.5

escape speed (235 m s^{-1}), which implies that most of the particles are falling back to the surface.

Our model implies that only ~1% of the upward-moving particles escape to supply the E ring. For an assumed particle radius of 1 μm, the inferred escape rate is ~10^{13} s^{-1}, which is only twice the value estimated by the Cosmic Dust Analyzer (CDA), 5 × 10^{12} s^{-1}, for particles with radii $r \geq 2$ μm (*15*). The closeness of these two numbers is surprising because ISS, which is sensitive at high phase angles to particles as small as 0.1 μm, is probably seeing a large population of particles smaller than 2 μm that CDA does not see. Our mass escape rate is ~0.04 kg s^{-1}, 4% of that estimated to supply the E ring using pre-Cassini parameters for both the plasma environment and the E-ring optical depth (*31*). Cassini has found temporal variability in the neutrals and plasma environment around Saturn, so the E-ring supply rate is uncertain. Also, our estimate is uncertain, first because it relies on an assumed particle size distribution, and second because it is sensitive to the exponential tail of the velocity distribution. Future Cassini observations in an extended mission should allow better imaging of the extended plume and a more accurate measure of the escape rate. At the moment, we interpret these observations to indicate that the south polar jets are the primary source of the E ring. The fact that almost all of the observed particles in the jets and extended plume are falling back to the surface may explain the extreme brightness of the interstripe plains as being due to freshly fallen snow (Fig. 3A).

According to our model fit to the observations, the particles that escape to supply the E ring have mean velocities of $\langle v \rangle$ ~ 90 m s^{-1} after they leave the gravity field of Enceladus. Particles injected vertically into Saturn's orbit from Enceladus' south pole with such velocities will have full vertical excursions (above and below the equatorial plane) on the order of $h \sim \langle v \rangle P/\pi$, where P is the orbital period (1.37 days) of Enceladus, or h ~ 3400 km. This is comparable to the vertical extent of the E ring at the orbit of Enceladus, ~5000 km, as measured in Cassini ISS images (*32*), and argues in favor of the south polar jets on Enceladus being the source of the E ring.

Plume dynamics. What do Cassini observations imply about the physical conditions within the jets and at their source? There are two basic possibilities for the source of the jets: either sublimating ice, above or below ground, or underground reservoirs of boiling liquid erupting through vents in the tiger stripes. The former operates at temperatures below 273 K; the latter operates above 273 K. We consider both in order.

The Ultraviolet Imaging Spectrograph (UVIS) observation of the occultation by Enceladus of γ-Orionis (*17*) returned an estimated horizontal column abundance of water vapor, within 30 km of the surface near 76°S (Fig. 1), of 1.5 × 10^{20} molecules m^{-2}. The mass of water vapor in the column is therefore 7.16 × 10^{-6} kg m^{-2}. At an equivalent location of ~15 km above a latitude of 76°S in the high-resolution November ISS images, we measured a horizontal particle column abundance of ~6 × 10^{8} m^{-2}, assuming an effective water-ice particle radius of 1 μm and a broad distribution of sizes (*30*). The mass of ice in the column is therefore ~3 × 10^{-6} kg m^{-2}, which is comparable to the mass of water vapor, assuming the UVIS and ISS horizontal paths are the same. The large ice/gas ratio argues strongly against ice condensing out of vapor, as would be expected for the sublimating ice model: The entropy change when the vapor condenses is ~20 times the entropy change when the same amount of vapor expands, so only a small fraction of the vapor can condense during an adiabatic expansion.

The grains could be embedded in the ice from the start and get entrained in the flow, like the dust grains in a comet, but this seems unlikely. The grains in comets are refractory and eventually cover the comet's surface with a dark crust. In contrast, the surface of Enceladus is bright and is mostly water ice. In particular, the spectrum of the plains between the tiger stripes (fig. S1) indicates that the plume particles falling back onto the

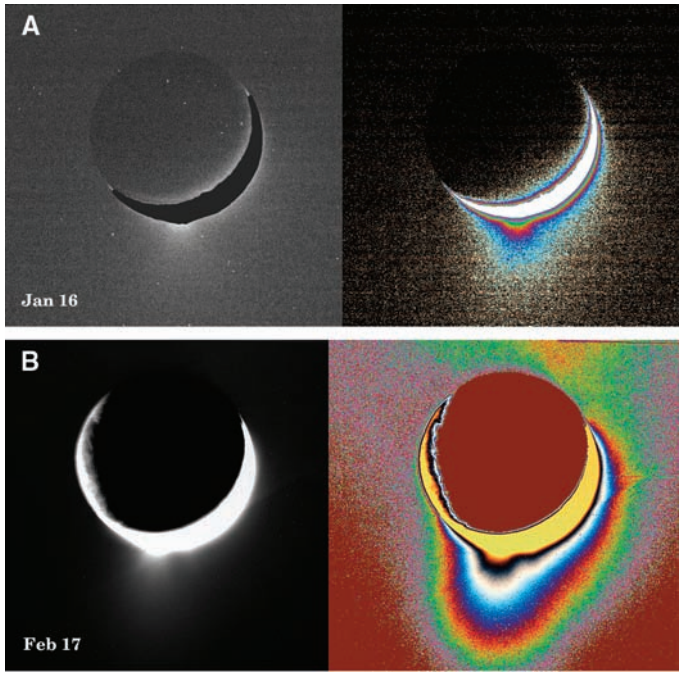

Fig. 5. False-color ISS NAC images of Enceladus' plumes (**A**) A NAC image taken in the IR1 filter (*12*) on 16 January 2005 at a phase angle of 148° with an image scale of ~1.25 km/pixel, showing a plume extending below the southern limb. Its full width at half maximum (FWHM) brightness and an altitude of 25 km was ~60 km. The subspacecraft latitude was –2.6°; the view is toward 133°W longitude (Fig. 1) and broadside to the tiger stripes. (**B**) A NAC image taken in the IR1 filter (*12*) on 17 February 2005, at a phase angle of 153.3° with an image scale of 1.8 km/pixel. The subspacecraft latitude was +0.6°; the view is toward 238°W longitude, along the tiger stripes (Fig. 1). Two near-surface plumes can be seen extending below the southern limb: a large one [maybe the same as in (A)] with FWHM ~60 km, and a smaller one, about one-third as bright as the main plume and separated from it by ~100 km (~23° in the counterclockwise direction), with a FWHM of ~30 km. A fainter and much more extended component can be seen in the enhanced, color-coded image on the right. A thin camera artifact, crossing diagonally across Enceladus, can also be seen.

Table 2. Moments and values of ε (the ratio of libration frequency to spin frequency, $[3(B - A)/C]^{1/2}$) for four different interior models. Moments are relative to MR^2, where M is mass and R is the mean radius, about axes a, b, and c. Shape model radii are 256.6 ± 0.5, 251.4 ± 0.2, and 248.3 ± 0.2 km. Uncertainties in model moments derive from ranges of shapes allowed by maximum change in a, b, and c.

Variable	Model 1 (homogeneous, 1608 kg m^{-3})	Model 2 (crust: 10.6 km ice, 930 kg m^{-3}; core 1700 kg m^{-3})	Model 3 (crust: 20.5 km ice, 930 kg m^{-3}; core 1800 kg m^{-3})	Model 4 (mantle 930 kg m^{-3}; core 2700 kg m^{-3})
A	0.3919 ± 0.0005	0.3785 ± 0.0005	0.3666 ± 0.0005	0.3138 ± 0.0005
B	0.4002 ± 0.0001	0.3865 ± 0.0001	0.3744 ± 0.0001	0.3205 ± 0.0001
C	0.4050 ± 0.0005	0.3911 ± 0.0005	0.3789 ± 0.0005	0.3243 ± 0.0005
ε	0.249 ± 0.014	0.248 ± 0.016	0.248 ± 0.017	0.249 ± 0.017

surface must be water ice. It is conceivable that ice grains, originally embedded in the ice matrix, get entrained in the flow, but this too seems unlikely. If no other gases are present, sintering will fuse micrometer-sized ice grains together in less than an hour, even at pressures as low as 1 Pa (*33*). Once fused to the matrix, the particles can no longer be entrained. The presence of micrometer-sized particles in the plume argues against entrainment in the sublimating ice model, but further study is needed.

On the other hand, there is no problem forming particles from a boiling liquid. A liquid boils when the pressure drops below its saturation vapor pressure. The erupting mixture of vapor and liquid—or, in the case of Enceladus, vapor, liquid, and ice particles—is like a cold Yellowstone geyser (*34*). Ammonia-water mixtures, although liquid down to 175 K, are ruled out as sources because the almost pure ammonia composition of the vapor is inconsistent with the observations (*16*). Therefore, any boiling liquid/geysers must involve pure water at 273 K or above. (Ammonia-water mixtures may be circulating underground and thermally conducting heat to the surface, keeping the tiger stripes warm, but these fluids cannot be venting to the surface.)

The boiling liquid can produce a cloud of gas and ice if some of the liquid is carried along with the vapor and freezes as it expands out of the vent. An H_2O mixture at the triple point has a temperature T = 273 K and a vapor pressure P_v = 612 Pa, corresponding to a hydrostatic head of 7 m in the weak gravity of Enceladus. When capped by a layer of ice, liquid water at this depth and temperature is in equilibrium with ice grains and vapor; at greater and warmer depths, the liquid is stable. If this pressure is released (e.g., when a crack forms in the ice), bubbles of vapor form and the liquid freezes. The heat of fusion (L_f = 6.0 kJ/mol) goes into heat of vaporization (L_v = 40.6 kJ/mol), and the mole fraction X of the vapor rises from zero to $L_f/(L_f + L_v)$ = 0.13. Although the mixture is then mostly ice, $1 - X$ = 0.87 by mole, its volume per mole is 24,000 times that of liquid water. In contrast, the expansion in a Yellowstone geyser is only a factor of ~10, and the water comes out as a frothy mixture.

When released from pressure, the source fluid will accelerate out of the vent as an ice/gas mixture. The geometry of the vent determines the angle of emergence and what fraction of the ice is in micrometer-sized particles. A gas expanding into vacuum reaches sonic speed, which for water vapor at 273 K is twice the escape velocity. Even water vapor at 200 K can accelerate micrometer-sized particles to escape velocity. Warmer, denser vapors can accelerate larger particles. Our inference, that most of the particles are falling back, implies that particles much larger than 1 μm are present. A boiling liquid at 273 K could produce copious amounts of large and small ice particles. The particles would retain the launch velocities and angles acquired in the conduit to form the collimated jets observed (Fig. 6A). There is no need to grow the particles from an escaping high-velocity gas or entrain them in the flow from the ice matrix. For these reasons, we favor the boiling liquid model over the sublimating ice model. On the basis of pressure arguments alone, the liquid chambers giving rise to Enceladus' geysers could be as close as 7 m to the surface.

Discussion. How to get liquid water close to the surface on Enceladus is a difficult question. Because previous interior thermal models for Enceladus cannot explain the anomalous heating seen in the SPT, we cannot exclude the possibility that the processes producing the observed heating might result in local regions with even higher temperatures, leading to subsurface reservoirs of liquid water. In this model, heating large enough to raise the temperature to 273 K might be provided by very localized, near-surface tidal and/or librational frictional heating operating on and within the tiger stripe fractures, as has been suggested for Europa (*35*), although detailed models for Enceladus have not been investigated.

Our proposed models for plume sources imply large temperatures near the surface. Because warm water ice can deform relatively easily by viscous creep over short geological times, we have investigated the implications of such elevated near-surface temperatures for the observed small-scale topography (e.g., 100-m ridges bounding fractures 500 m deep) on the satellite's surface. We have applied models using rheologic parameters from a recent exploration of superplastic flow assuming grain boundary–sliding basal slip in ice under low stress (*36*) and considering a grain size of 100 μm, equal to that inferred for the tiger stripes. Assuming a background temperature of the SPT of ~95 K and liquid reservoirs at depths between 0.5 and 1 km for ammonia-water at 175 K and 1 to 2 km for water at 273 K (i.e., a large geothermal gradient), finite element modeling shows that ~1-km topography would undergo measurable deformation on time scales of a few million to tens of millions of years. Very shallow liquid layers in regions outside the SPT are probably inconsistent with the retention of the observed topography there for the inferred lifetimes (from cratering statistics) of a billion years or more

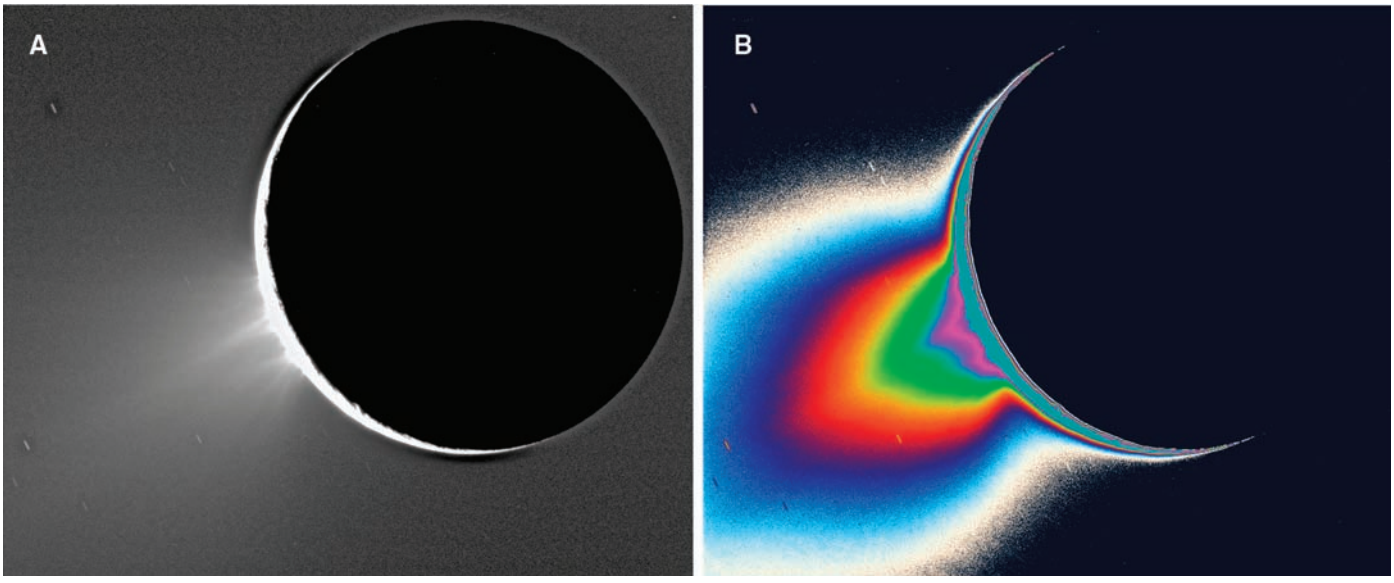

Fig. 6. (**A**) An ISS NAC clear-filter image (*12*) of Enceladus' near-surface plumes (which can be resolved into individual jets) taken on 27 November 2005 at a phase angle of 161.4° with an image scale of ~0.89 km/pixel. The subspacecraft latitude was +0.9°; the view on this day was also broadside to the tiger stripes (Fig. 1). The south pole is pointing toward the lower left. (**B**) A color-coded version of (A), in which faint light levels were assigned different colors to enhance visibility, shows the enormous extent of the fainter component above the south polar region.

(Table 1). Thus, Enceladus' subsurface structure may be globally heterogeneous, with some regions retaining a cold, thick upper crust for some time and the SPT being the only region where liquid may be close to the surface at the present time.

Tidal heating associated with the eccentricity of Enceladus' orbit, forced by its 2:1 mean motion resonance with Dione, has long been suspected (*37*). Using Cassini values for the mass (*27*), volume and mean density (this paper), and the current value of the orbital eccentricity $e = 0.0047$, we calculate a tidal heating rate of 1.2×10^{15} ergs s^{-1} for a homogeneous model and an assumed tidal dissipation parameter $Q = 20$: The lower the value of Q, the more dissipative the interior.

Enceladus' rotation state is important when considering possible heating inputs from the 1:4 secondary resonance librations. For Enceladus to be librating with an amplitude equal to the measured upper limit (1.5°), ε must equal 0.25005 for the current orbital eccentricity, well within the uncertainties of the measured ε for all homogeneous and differentiated models. This would yield a present-day heating rate due to secondary libration alone of 1.8×10^{15} ergs s^{-1}, again for $Q = 20$.

The Cassini value of mass density for Enceladus implies a rock fraction ($mass_{rock}/mass_{Enc}$) of 0.61. This higher rock fraction, plus the higher mass, compared to the values derived from Voyager data, imply an increase of a factor of 2.5 in the total rock mass over Voyager-based estimates. Thus, we can expect the present-day radiogenic heating rate to be equivalently higher, 3.2×10^{15} ergs s^{-1}, assuming chondritic long-lived radionuclide abundances (*38*). The present-day total heating rate on Enceladus from all aforementioned sources, assuming $Q = 20$, could be 4×10^{15} to 6×10^{15} ergs s^{-1}, or ~0.5 GW, about one-tenth the observed total power coming from the SPT (*13*). However, this heating rate might be significantly enhanced for more realistic viscoelastic models of the interior.

Previous models (*5*) have suggested that the present tidal heating from eccentricity forcing by the resonant perturbations of Dione alone, although not enough to initiate melting, might be sufficient to maintain as liquid a portion of an icy interior as near to the surface as 10 km, if the start of melting had occurred in a previous epoch and if the melting point were depressed by mixing a substantial amount of ammonia with water in the ice (*8*). Also, calculations (*39*) using the older heating estimates but differentiated interiors show that a mantle temperature of 210 K could be within 10 km of the surface for specific rheological parameterizations. The higher radiogenic heating indicated by Cassini results (2.5 times as much energy as used in pre-Cassini models) and the possibility of additional present-day librational heating suggest that some interior liquid is even more likely than in previous models, assuming ammonia is present, and may be possible within tens of kilometers of the surface in differentiated models without invoking large amounts of ammonia. Although no instrument has positively detected ammonia, its existence cannot be ruled out: The derived upper limiting value to the ammonia abundance [0.5% in the plume vapor (*16*)] could still permit a geophysically important amount of ammonia at depth, although, as discussed above, an ammonia-water mixture cannot be venting to space. It is also possible, as mentioned above, that a pure-water interior heated preferentially on fractures as for Europa (*35*) might retain near-surface liquid water up to the present in localized regions. Consequently, it is plausible that Enceladus may be sufficiently heated today by some combination of the mechanisms mentioned above to explain the observed south polar venting, provided it underwent an early epoch of intense heating and, once heated, retained a low Q up through the present in some portion of the interior. Explaining the observed power output of 5 GW (*13*) is more challenging.

How was Enceladus initially heated? Previous suggestions (*5*) calling for a larger orbital eccentricity in the past to increase tidal heating are not attractive: Not only is considerable past orbital evolution not likely, but capture into the 2:1 mean motion Dione resonance through tidal evolution does not produce a past eccentricity larger than Enceladus' current value. If, instead, the moon was at one time in the 1:4 secondary libration resonance, as the observed value of $\varepsilon \sim 0.25$ suggests, how did it get captured, and could heating from this mechanism have been sufficient for melting? Wisdom (*9*) discussed several scenarios for placing Enceladus in a spin-orbit secondary resonance. One possibility is an impact that initiated libration and allowed capture into the 1:4 resonance. An initial $\varepsilon = 0.26$, with an associated libration amplitude of 22°, yields a heating rate 100 times that due to the forced eccentricity today for typical fully elastic models and the same temperature-independent $Q = 20$. For more realistic temperature-dependent viscoelastic models of the interior and a long residence time in this resonance, considerable initial heating may be possible, although detailed models have not yet been examined.

It is easy to see how strong heating from a large past libration could completely relax the body, reducing ε to < 0.26, damping the libration, and thus terminating the spin-orbit secondary resonance, resulting in a hydrostatic shape. However, the uncertainties allow the possibility that the shape may be nonhydrostatic and ε may be as high as 0.26 (Table 2). A nonhydrostatic shape and a present-day $\varepsilon \sim 0.26$ could be explained if Enceladus were in the 1:4 resonance in the past, and internal heating of the moon was insufficient to bring about full differentiation and hydrostatic equilibrium but still served to decrease Q, increase dissipation, and damp the resonance. Moreover, if this heating were nonuniform within the body, as Cassini observations show, the figure might have evolved in unusual ways, relaxing in some regions and not others, yet remaining overall close to its original figure and original ε despite the damping of the libration.

These changes in figure might have left discernible marks on the surface. The symmetry and distribution of young tectonic patterns, especially those associated with the SPT, suggest that Enceladus may have undergone large-scale changes of figure over time. The north-south–trending fractures and rifts that extend northward from the south polar Y-shaped discontinuities (Fig. 2D) appear to have formed in response to horizontal extensional stresses aligned along circles of latitude. Such parallel "hoop" stresses near equatorial latitudes could arise in response to an increase in flattening of the figure of Enceladus (*40*, *41*).

Moreover, the appearance and symmetry of the SPT boundary at ~55°S latitude identify a change in the character of stresses associated with global deformation. Here, the change in orientation of the Y-shaped discontinuities, from north-south–trending nearer the equator to east-west–trending along the south polar margin, imply a change in principal tensile stresses that caused the fracturing, from strong tensile stresses parallel to the equator at equatorial latitudes to predominantly compressional stresses perpendicular to circles of latitude at the SPT boundary. The sinuous belts of ridges and troughs at the SPT margin were probably formed in response to horizontal compressive stresses perpendicular to circles of latitude. A transition in the character of horizontal stresses with increasing latitude is also expected to accompany an increase of flattening in Enceladus' figure (*40*, *41*).

Two problems with this "figure flattening" interpretation are (i) the absence of similar circumpolar features and tectonic fractures in the north polar region, indicating that the putative alteration in shape was not global, and (ii) the lack of any plausible mechanism for increased flattening. We note that the observed asymmetric distribution of heat within the body may explain the surface expression of global stresses in one hemisphere and not the other. These are suggestions that remain to be investigated in detail. The tiger stripe fractures in the SPT, and their ~45° orientation with respect to the Saturn direction, suggest tidal deformation or some other process as another contributing factor in the tectonic patterns characterizing the SPT.

References and Notes

1. A. J. Verbiscer, R. G. French, C. A. McGhee, *Icarus* **173**, 66 (2005).
2. D. P. Cruikshank, *Icarus* **41**, 246 (1980).
3. K. D. Pang, C. C. Voge, J. W. Rhoads, J. M. Ajello, *J. Geophys. Res.* **89**, 9459 (1984).
4. B. A. Smith *et al.*, *Science* **212**, 163 (1981).
5. S. W. Squyres, R. T. Reynolds, P. M. Cassen, S. J. Peale, *Icarus* **53**, 319 (1983).

6. J. S. Kargel, S. Pozio, *Icarus* **119**, 385 (1996).
7. J. Lewis, *Icarus* **15**, 174 (1971).
8. S. J. Peale, *Annu. Rev. Astron. Astrophys.* **37**, 533 (1999).
9. J. Wisdom, *Astron. J.* **128**, 484 (2004).
10. M. K. Dougherty *et al.*, *Science* **311**, 1406 (2006).
11. R. H. Brown *et al.*, *Science* **311**, 1425 (2006).
12. C. C. Porco *et al.*, *Space Sci. Rev.* **115**, 363 (2004).
13. J. R. Spencer *et al.*, *Science* **311**, 1401 (2006).
14. ISS and CIRS are acknowledged in the codiscovery of the correlation between the hottest temperatures measured in the SPT and the tiger stripe fractures.
15. F. Spahn *et al.*, *Science* **311**, 1416 (2006).
16. J. H. Waite Jr. *et al.*, *Science* **311**, 1419 (2006).
17. C. J. Hansen *et al.*, *Science* **311**, 1422 (2006).
18. G. H. Jones *et al.*, *Science* **311**, 1412 (2006).
19. G. Hansen, personal communication.
20. C. C. Porco *et al.*, *Science* **307**, 1237 (2005).
21. G. Neukum *et al.*, *Lunar Planet. Sci. Conf. 36*, abstract 2034 [CD-ROM] (2005).
22. R. Wagner *et al.*, *Bull. Am. Astron. Soc.* **37**, 701 (2005).
23. G. Neukum, thesis, Ludwig-Maximilians-Universität München (1983).
24. G. P. Horedt, G. Neukum, *J. Geophys. Res.* **89**, 10405 (1984).
25. G. Neukum, *Adv. Space Res.* **5**, 107 (1985).
26. R. Ionasescu, *Jet Propulsion Laboratory Interoffice Memorandum IOM 343J-05-017* (2 May 2005).
27. R. Jacobson and the Cassini Project Navigation team, personal communication.
28. S. F. Dermott, *Icarus* **37**, 575 (1979).
29. S. F. Dermott, P. C. Thomas, *Icarus* **109**, 241 (1994).
30. Brightness values were converted into particle densities with the use of an assumed analytical particle size distribution (*42*): $n(r)$ = constant $r^{(1-3b)/b}$ exp(–r/ab), where a is the effective radius (1.0 μm, appropriate for particles in the E ring) and b = 0.25. The quantity b is large enough to ensure a fair fraction of the particles are large enough (i.e., >2 μm) for CDA to detect. Horizontal (line-of-sight) column densities, N_{los}, were computed from the peak I/F by the relation N_{los} = 4(I/F)/[A_{sca} × $P(\varphi)$], where A_{sca} is the scattering cross section appropriate for the chosen particle size distribution, and $P(\varphi)$ is the phase function computed for Mie scatterers at phase angle φ. The scattering cross section used for the assumed particle size distribution and an effective observation wavelength of 569 nm was 3.12 square μm; $P(\varphi = 161.4)$ = 6.688.
31. A. Juhasz, M. Horanyi, *J. Geophys. Res.* **107**, A6 1066 (2002).
32. M. Hedman, personal communication.
33. J. Eluszkiewicz, J.-L. Moncet, *Icarus* **166**, 375 (2003).
34. S. W. Kieffer, in *The Satellites of Jupiter*, D. Morrison, Ed. (Univ. of Arizona Press, Tucson, AZ, 1982), pp. 647–723.
35. E. J. Gaidos, F. Nimmo, *Nature* **405**, 637 (2000).
36. D. L. Goldsby, D. L. Kohlstedt, *J. Geophys. Res.* **106**, 11017 (2001).
37. C. F. Yoder, *Nature* **279**, 767 (1979).
38. G. Schubert, T. Spohn, R. T. Reynolds, in *Satellites*, J. A. Burns, M. S. Matthews, Eds. (Univ. of Arizona Press, Tucson, AZ, 1986), pp. 224–292.
39. M. N. Ross, G. Schubert, *Icarus* **78**, 90 (1989).
40. P. Helfenstein, E. M. Parmentier, *Icarus* **53**, 415 (1983).
41. H. J. Melosh, *Icarus* **31**, 221 (1977).
42. J. E. Hansen, *J. Atmos. Sci.* **28**, 1400 (1971).
43. G. Neukum, B. A. Ivanov, W. K. Hartmann, *Space Sci. Rev.* **96**, 55 (2001).
44. K. Zahnle, P. Schenk, H. Levison, L. Dones, *Icarus* **163**, 263 (2003).

45. We acknowledge the financial support of NASA/JPL, the UK Particle Physics and Astronomy Research Council, the Deutsches Zentrum fur Luft- und Raumfahrt (German Aerospace Center), and Université Paris VII Denis Diderot, Commissariat à l'Energie Atomique, Astrophysique Interactions Multieschelle, France.

Supporting Online Material

www.sciencemag.org/cgi/content/full/311/5766/1393/DC1
Fig. S1

25 November 2005; accepted 21 February 2006
10.1126/science.1123013

RESEARCH ARTICLE

Cassini Encounters Enceladus: Background and the Discovery of a South Polar Hot Spot

J. R. Spencer,[1]* J. C. Pearl,[2] M. Segura,[2] F. M. Flasar,[2] A. Mamoutkine,[2] P. Romani,[2] B. J. Buratti,[3] A. R. Hendrix,[3] L. J. Spilker,[3] R. M. C. Lopes[3]

The Cassini spacecraft completed three close flybys of Saturn's enigmatic moon Enceladus between February and July 2005. On the third and closest flyby, on 14 July 2005, multiple Cassini instruments detected evidence for ongoing endogenic activity in a region centered on Enceladus' south pole. The polar region is the source of a plume of gas and dust, which probably emanates from prominent warm troughs seen on the surface. Cassini's Composite Infrared Spectrometer (CIRS) detected 3 to 7 gigawatts of thermal emission from the south polar troughs at temperatures up to 145 kelvin or higher, making Enceladus only the third known solid planetary body—after Earth and Io—that is sufficiently geologically active for its internal heat to be detected by remote sensing. If the plume is generated by the sublimation of water ice and if the sublimation source is visible to CIRS, then sublimation temperatures of at least 180 kelvin are required.

Cassini-Huygens is a major international planetary mission that entered orbit around Saturn on 1 July 2004 for a nominal 4-year investigation of the planet, its satellites, rings, and magnetosphere. In 2005, Cassini made three flybys of the enigmatic satellite Enceladus, long suspected to be recently geologically active and the source of Saturn's tenuous, extended E ring. Results from multiple Cassini instruments on the third flyby on 14 July 2005 offer convincing proof that this small icy satellite is currently active, as described in this series of companion papers.

Enceladus. Discovered by William Herschel in 1789, Enceladus orbits close to Saturn at a radius of 3.94 Saturn radii and thus is difficult to observe from Earth because of the scattered light of the planet and its rings. Enceladus' orbital period is 1.37 days. Telescopic infrared spectra indicate a surface composed of almost pure water ice (*1*), although a tentative detection of ammonia ice has been reported recently (*2*). The Voyager encounters with the satellite in 1981 established its radius (252.1 km) (*3*) and that its visual geometric albedo is startlingly high, consistent with fresh snow or ice, and higher than for any other known solar system body (*4*, *5*). Voyager 2 also discovered that Enceladus was unique among Saturn's medium-sized icy satellites, because its surface includes sizable crater-free areas that have been resurfaced by endogenic forces (*4*) and were estimated to be <200 million years old (*6*). Other parts of the satellite are heavily cratered and perhaps nearly as old as the solar system, but the craters show considerable signs of internal modification. All regions of the satellite, regardless of age, exhibit uniformly high albedos, implying that the entire satellite is coated with a ubiquitous fresh material (*7*). Particle-orbit models have shown that Enceladus is probably the major source of the tenuous E ring (*8*), which is most dense at the satellite's orbit. The mechanism for the injection of material from the satellite into the E ring has been debated; volcanism (*9*), geysers (*10*), large impacts (*11*), and collisions between Enceladus and E-ring particles themselves (*12*) have all been proposed. Regardless of the means of transport, the micrometer-sized particles that make up the ring must be constantly replenished, because sputtering (*10*, *13*) would destroy them on time scales much shorter than the age of the solar system.

The heat source for the extensive resurfacing on an object as small as Enceladus has always been difficult to explain, especially when compared to other saturnian satellites that show much less evidence of activity (*14*–*16*). The orbital eccentricity of Enceladus (0.0047, comparable to that of Io) is perhaps sufficient for substantial

[1]Department of Space Studies, Southwest Research Institute, 1050 Walnut Street, Suite 400, Boulder, CO 80302, USA. [2]NASA Goddard Spaceflight Center, Code 693, Greenbelt, MD 20771, USA. [3]Jet Propulsion Laboratory, California Institute of Technology, 4800 Oak Grove Drive, Pasadena, CA 91109, USA.

*To whom correspondence should be addressed. E-mail: spencer@boulder.swri.edu